

Recovering missing data in coherent diffraction imaging

D. A. Barmherzig¹, A.H. Barnett¹, C.L. Epstein^{1,2}, L.F. Greengard^{1,3},
J.F. Magland¹, and M. Rachh¹

¹Center for Computational Mathematics, Flatiron Institute, New York, NY

²Department of Mathematics, University of Pennsylvania

³Courant Institute, New York University

December 16, 2021

Abstract

In coherent diffraction imaging (CDI) experiments, the intensity of the scattered wave impinging on an object is measured on an array of detectors. This signal can be interpreted as the square of the modulus of the Fourier transform of the unknown scattering density. A beamstop obstructs the forward scattered wave and, hence, the modulus Fourier data from a neighborhood of $\mathbf{k} = \mathbf{0}$ cannot be measured. In this note, we describe a *linear* method for recovering this unmeasured modulus Fourier data from the measured values and an estimate of the support of the image's autocorrelation function *without* consideration of phase retrieval. We analyze the effects of noise, and the conditioning of this problem, which grows exponentially with the modulus of the maximum spatial frequency not measured.

Keywords: Coherent diffraction imaging, hole in \mathbf{k} -space, autocorrelation image, recovered magnitude data, noise.

1 Introduction

In coherent diffraction imaging (CDI) experiments, the intensity of the scattered wave impinging on an object is measured on an array of detectors. This signal can be interpreted as the square of the modulus of the Fourier transform $|\hat{\rho}(\mathbf{k})|^2$ of the unknown scattering density, denoted by $\rho(\mathbf{x})$ [15, 7]. The spatial frequency, \mathbf{k} , is related to the scattering direction through the Ewald sphere construction [8]. We assume here that the x-ray wavelength is sufficiently small that the curvature of

the Ewald sphere can be neglected and that we are sampling $|\widehat{\rho}(\mathbf{k})|^2$ on a uniform grid. The *phase retrieval problem* is to recover the complex values $\widehat{\rho}(\mathbf{k})$, and hence the desired unknown, from the measured intensity data, supplemented by auxiliary information, which is typically the approximate support of $\rho(\mathbf{x})$ [4, 18, 2]. Unfortunately, a *beamstop* obstructs the forward scattered wave and, hence, the modulus Fourier data from a neighborhood of $\mathbf{k} = \mathbf{0}$ cannot be measured. Standard iterative approaches to recovering the unmeasured samples, such as HIO or difference maps [10, 12], use the auxiliary information to fill in the unmeasured Fourier coefficients at the same time as the image itself is reconstructed. In this note, we describe a *linear* method for recovering this unmeasured modulus Fourier data from the measured values and an estimate of the support of the image's autocorrelation function, *without* consideration of phase retrieval.

To set various parameters and length scales, we assume that ρ is supported in a compact subset of $\mathcal{S} = (-\frac{1}{2}, \frac{1}{2})^d$, and that its autocorrelation image

$$(\rho \star \rho)(\mathbf{y}) \equiv \int_{\mathcal{S}} \rho(\mathbf{x}) \rho(\mathbf{y} + \mathbf{x}) d\mathbf{x}$$

is supported in $(-\frac{\beta}{2}, \frac{\beta}{2})^d$. We define the *field of view* (FOV) as the box $(-\frac{m}{2}, \frac{m}{2})^d$ (Fig. 1).

The Fourier transform, $\widehat{\rho}$, is defined by

$$\widehat{\rho}(\mathbf{k}) \equiv \int_{\mathbb{R}^d} \rho(\mathbf{x}) e^{-2\pi i \mathbf{x} \cdot \mathbf{k}} d\mathbf{x}, \quad (1)$$

so that

$$\rho(\mathbf{x}) \equiv \int_{\mathbb{R}^d} \widehat{\rho}(\mathbf{k}) e^{2\pi i \mathbf{x} \cdot \mathbf{k}} d\mathbf{k}. \quad (2)$$

Finally, we assume that $|\widehat{\rho}(\mathbf{k})|^2$ is given in the box \mathcal{D} of side length $2K_{max}$, from which a window $\mathcal{W} = [-k_0, k_0]^d$ is deleted, corresponding to the beamstop (Fig. 1).

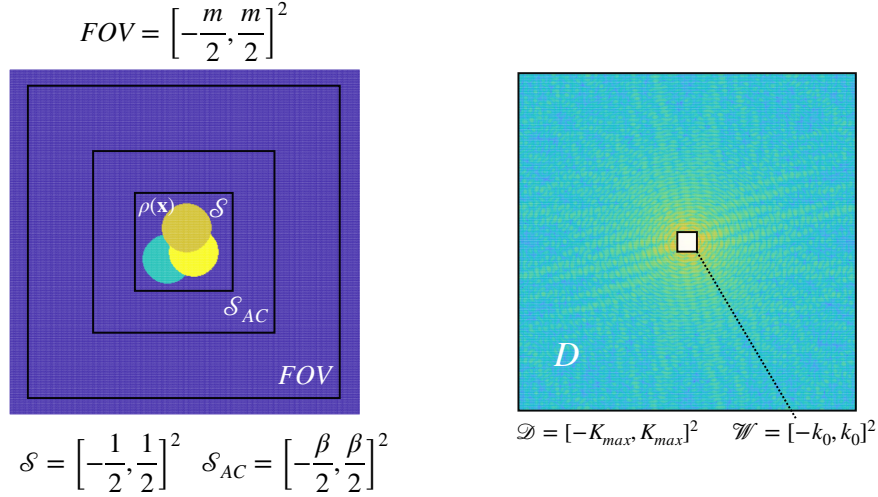


Figure 1: A two-dimensional object of interest $\rho(\mathbf{x})$ is supported in the bounded region $\mathcal{S} = [-\frac{1}{2}, \frac{1}{2}]^2$ and its autocorrelation is supported in $\mathcal{S}_{AC} = [-\frac{\beta}{2}, \frac{\beta}{2}]^2$. The field of view (FOV) is the maximum region in physical space where we expect the Fourier transform (2) to be valid for a given sampling of $\hat{\rho}(\mathbf{k})$. We denote by R the subset of the field of view outside \mathcal{S}_{AC} . In the transform domain (k -space), the modulus of $\hat{\rho}(\mathbf{k})$ is measured on a box \mathcal{D} , with the region \mathcal{W} obscured by the beamstop.

For the sake of simplicity, we work in the discrete setting, with

$$\rho_{\mathbf{j}} = \rho\left(\frac{\mathbf{j}}{2N}\right), \text{ for } \mathbf{j} \in [1 - N : N]^d. \quad (3)$$

From the Nyquist sampling theorem, the grid spacing $\frac{1}{2N}$ in physical space corresponds to a maximum frequency in the transform domain of $K_{max} = N$. Following Fig. 1, we define $J = [1 - mN : mN]^d$, in order to cover the field of view. The vector $\boldsymbol{\rho} \in \mathbb{R}^J$, is of length $(2mN)^d$, and has entries defined by (3) for $\mathbf{j} \in [1 - N : N]^d$ and zero otherwise, corresponding to the fact that $\rho(\mathbf{x})$ is supported in \mathcal{S} . In taking the discrete Fourier transform of $\boldsymbol{\rho}$ with a fixed N , increasing values of m lead to a finer sampling of $\hat{\rho}$ in the transform domain, without changing the maximum frequency $K_{max} = N$. As a result, we sometimes refer to $m > 1$ as the “oversampling” factor. In the CDI experiment, oversampling corresponds to using an array of sensors that measure $|\hat{\rho}(\mathbf{k})|$ on a grid with spacing $\Delta k = 1/m$. This is the Nyquist sampling rate in the inverse direction, sufficient to recover a physical object *within the field of view*. It is the combination of oversampling with

prior information about the support of $\rho(\mathbf{x})$ that makes the phase retrieval problem solvable, for a dense open set of data, in dimensions $d > 1$ [6, 14].

In the remainder of this paper, we let

$$\hat{\rho}_{\mathbf{k}} \equiv \sum_{j \in J} \rho_j e^{-\frac{2\pi i j \cdot \mathbf{k}}{2mN}} \approx (2N)^d \hat{\rho}\left(\frac{\mathbf{k}}{m}\right) \quad (4)$$

denote the discrete Fourier transform (DFT) of the data extended by zero to the entire field of view. Thus, in our model problem, the measured intensity is proportional to $(|\hat{\rho}_{\mathbf{k}}|^2)$. We also recall the well-known fact that $(|\hat{\rho}_{\mathbf{k}}|^2)$ is the DFT of the discrete (periodic) autocorrelation image:

$$(\rho \star \rho)_{\mathbf{k}} \equiv \sum_{j \in J} \rho_j \rho_{j+\mathbf{k}}.$$

Let $W \subset J$ denote the set of lattice points obstructed by the beamstop \mathcal{W} . Substantial effort has been devoted to the development of methods for approximating the Fourier coefficients at these frequencies. Typically, this involves an iterative method designed to solve the phase retrieval problem and missing data problem simultaneously (see, for example, [17, 9].) In Section 2 we describe a linear algorithm for recovering the unmeasured values $\{|\hat{\rho}_{\mathbf{k}}|^2 : \mathbf{k} \in W\}$. It amounts to solving a least squares problem for the unmeasured coefficients, using knowledge about the support of the autocorrelation of ρ as a constraint. In Section 3 we analyze the conditioning of this problem, by relating it to classical results for prolate spheroidal functions, see [20]. We show that if $|W|$ is not too large, then, with sufficiently fine sampling in the Fourier domain, e.g. $m \geq 3$, the unmeasured magnitude data, $\{|\hat{\rho}_{\mathbf{k}}|^2 \text{ for } \mathbf{k} \in W\}$, can be stably determined by solving the least squares problem (Fig. 2).

While \mathcal{W} (and \mathcal{S}_{AC}) can, in principle take any shape, we assume for simplicity that it is square so that the lattice points lying within \mathcal{W} are of the form $W = [1-w : w-1]^d$, where $w = \lfloor 1 + mk_0 \rfloor$. With the discretized autocorrelation image $\rho \star \rho$ supported in $[-\beta N : \beta N]^d$, connections with prolate spheroidal functions show that asymptotically, as m, N , and βk_0 grow large, the conditioning of the linear method grows like

$$\kappa(\beta, k_0) \sim \frac{e^{\pi \beta k_0}}{\sqrt{4\pi d} [\beta k_0]^{\frac{1}{4}}}. \quad (5)$$

This estimate is proven in Appendix A. Empirically this asymptotic result is already accurate for $N \geq 128, m \geq 3$. The main lessons of (5), and the examples in Section 4, are

1. The conditioning of the hole filling problem is largely determined by the *physical* space-bandwidth product βk_0 .
2. Little can be gained in this context by taking either $m \geq 4$, or N very large (neither parameter appears in the formula).
3. As the dimension, d , increases the conditioning can be expected to slightly improve; in particular, the exponent in (5) does *not* depend on d .

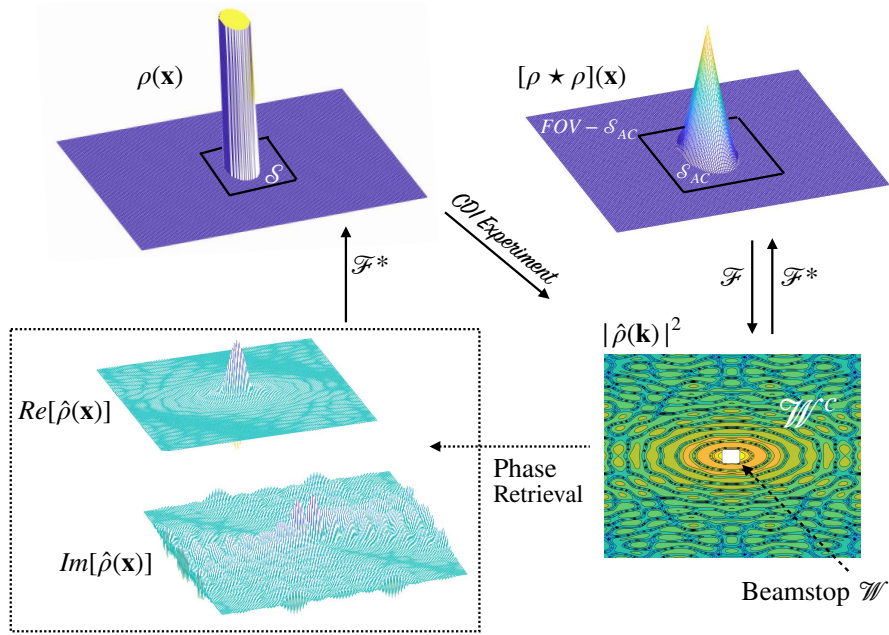


Figure 2: An unknown object $\rho(\mathbf{x})$ is supported in a bounded region \mathcal{S} (upper left) and its autocorrelation is supported in \mathcal{S}_{AC} (upper right). In standard methods for phase retrieval from CDI experiments, the missing data within the beamstop \mathcal{W} is inferred as part of an overall iterative scheme. Here, we solve for the missing data itself, without consideration of phase, by using an estimate for the support of the autocorrelation image and solving a linear least squares problem.

The effects of noise are analyzed in Sections 5–6, where it is shown that, if βk_0 is not too large, then, with sufficient SNR, this scheme can be robust even in the presence of noise. At lower SNR, we show that improved images may result if some of the reconstructed modulus data is used, and some of the coefficients are found implicitly in the phase retrieval step.

2 The Recovery Algorithm

In our model, the measured data, denoted by \mathbf{a}^2 , consists of

$$a_j^2 = \begin{cases} |\hat{\rho}_j|^2 & \text{for } j \in W^c = J \setminus W \\ 0 & \text{for } j \in W. \end{cases} \quad (6)$$

In the image domain, let $S \subset [1 - N : N]^d \subset J$ be the lattice points within our estimate for the support of ρ , then

$$S_{AC} = S \ominus S = \{j - k : j, k \in S\},$$

is an estimate for the support of the autocorrelation image S_{AC} , and set $R = J \setminus S_{AC}$. If $|R| > |W|$, then, in principle, the unmeasured magnitude data can be determined. For this problem to be reasonably well conditioned the ratio $|W|/m^d$ must be sufficiently small, and $|R| \gg |W|$. Empirically, a little more oversampling ($m = 3$) than is required for the phase retrieval problem to be solvable ($m = 2$) produces markedly better results. Having more samples also leads to better noise reduction when recovering the unmeasured samples. On other hand, greater oversampling may require a smaller pixel size on the detector, or a more distant detector, either of which would tend to increase the noise content of individual measurements, so clearly there are trade-offs to be considered. Our asymptotic analysis, and numerical examples indicate that there is little improvement beyond $m = 4$.

Let \mathcal{F} denote the d -dimensional DFT matrix, normalized to be a unitary operator, and let \mathcal{F}^* be its adjoint. To keep the notation simpler, we omit the spatial dimension d when the context is clear. We interpret \mathcal{F} as a map from data on the $|J|$ -point grid in the physical domain to a $|J|$ -point grid in the frequency domain, both contained in \mathbb{Z}^d . The frequency domain grid is normalized to be centered on $k = 0$. In the remainder of the paper we let $\hat{\rho}_k = [\mathcal{F}(\rho)]_k$, which differs, by the constant factor, $[2mN]^{-\frac{d}{2}}$, from the normalization in (4).

Definition 1. We denote by $\mathcal{F}_{W,R}$ the submatrix of \mathcal{F} that maps data from grid points in R to Fourier transform points in W . $\mathcal{F}_{W,S_{AC}}$ is the submatrix that maps data from grid points in S_{AC} to Fourier transform points in W . $\mathcal{F}_{W^c,R}$ and $\mathcal{F}_{W^c,S_{AC}}$ are defined in the same manner, as are the submatrices of the adjoint: $\mathcal{F}_{R,W}^*$, $\mathcal{F}_{S_{AC},W}^*$, \mathcal{F}_{R,W^c}^* , $\mathcal{F}_{S_{AC},W^c}^*$.

Note that taking the adjoint interchanges the roles of the two subsets, e.g., $[\mathcal{F}_{W,R}]^* = \mathcal{F}_{R,W}^*$.

As noted above, the DFT coefficients of the autocorrelation image, $\rho \star \rho$, are $\{|\hat{\rho}_j|^2 : j \in J\}$ (the Wiener-Khinchin theorem). Let us now write the inverse DFT in block form:

$$\begin{pmatrix} \mathcal{F}_{R,W}^* & \mathcal{F}_{R,W^c}^* \\ \mathcal{F}_{S_{AC},W}^* & \mathcal{F}_{S_{AC},W^c}^* \end{pmatrix} \begin{pmatrix} \alpha_W \\ a_{W^c}^2 \end{pmatrix} = \begin{pmatrix} 0 \\ \rho \star \rho \end{pmatrix}, \quad (7)$$

where $a_{W^c}^2 = a^2$ restricted to W^c , is the measured data and α_W denotes the (unmeasured) coefficients α_j of a^2 for j restricted to W . Clearly, letting $\alpha_W = (|\hat{\rho}_j|^2)_{j \in W}$ yields a consistent solution of (7), since this is simply a restatement of the Wiener-Khinchin theorem. If we restrict our attention to the first row, we have the $|R| \times |W|$ linear system:

$$\mathcal{F}_{R,W}^* \alpha_W = -\mathcal{F}_{R,W^c}^* a_{W^c}^2. \quad (8)$$

This is shown schematically in Figure 2.

For small sets W and large sets R the system of equations $\mathcal{F}_{R,W}^* \alpha_W = 0$ has only the trivial solution $\alpha_W = \mathbf{0}$. Assuming that the data $a_{W^c}^2$ is exact, then the highly overdetermined system in (8) has the exact solution, $\alpha_W = (|\hat{\rho}_j|^2)_{j \in W}$, which is unique. For generic right hand sides, the equation $\mathcal{F}_{R,W}^* x = -\mathcal{F}_{R,W^c}^* y$, does not have an exact solution, and in the remainder of the paper we take x to be the solution to the least squares problem:

$$x_0 = \arg \min_x \|\mathcal{F}_{R,W}^* x + \mathcal{F}_{R,W^c}^* y\|_2, \quad (9)$$

which is also unique, as $\mathcal{F}_{W,R} \mathcal{F}_{R,W}^*$ is invertible. More precisely, we have

Theorem 1. *Suppose that $J = [1-M : M]^d$. If $W \subset [p : p+u] \times [1-M : M]^{d-1}$, and $R \supset [q : q+v] \times [1-M : M]^{d-1}$, with $v > u$, then $\mathcal{F}_{R,W}^* x = 0$ has only the trivial solution.*

Proof. Let $x \in \mathbb{R}^J$ be a vector, with support in W , that belongs to the null-space of $\mathcal{F}_{R,W}^*$, and let $X(z)$ be its Z -transform. For every frequency k , the adjoint DFT, \tilde{x}_k , equals $X(\omega_k)$, for ω_k an appropriate vector of points on the torus $(S_1)^d$. We can rewrite the Z -transform as

$$X(z) = \sum_{j' \in [1-M:M]^{d-1}} p_{j'}(z_1)(z_2, \dots, z_d)^{j'}.$$

Up to a factor of z_1^p , each $p_{j'}(z_1)$ is a polynomial of degree u .

The hypothesis of the theorem implies that for any $\omega_k = (\omega_{k_1}, \dots, \omega_{k_d})$ with $k_1 \in [q : q+u]$, we have that $X(\omega_k) = 0$. By the invertibility of the $(d-1)$ -dimensional DFT, this implies that $p_{j'}(\omega_{k_1}) = 0$ for all j' and $k_1 \in [v : q+v]$. Because $v > u$ and $p_{j'}$ are polynomials of degree u , this shows that the polynomials are actually all zero, which, in turn, implies that $x = \mathbf{0}$ as well. \square

As $|W|$ is a reasonably small number, the reduced SVD of

$$\mathcal{F}_{R,W}^* = U\Sigma V^*$$

is fairly easy to compute. The Moore-Penrose inverse of $\mathcal{F}_{R,W}^*$ is

$$\mathcal{F}_{R,W}^{*\dagger} = V\Sigma^{-1}U^*. \quad (10)$$

The unique solution to the overdetermined linear system in (8) is given by

$$\alpha_W = -\mathcal{F}_{R,W}^{*\dagger} \mathcal{F}_{R,W}^* \mathbf{a}_{W^c}^2. \quad (11)$$

We call the operator

$$\mathcal{R}_{R,W} = -\mathcal{F}_{R,W}^{*\dagger} \mathcal{F}_{R,W}^* \quad (12)$$

the *recovery operator*. For general right hand sides, \mathbf{y} , the solution to the least squares problem is given by $\mathcal{R}_{R,W}\mathbf{y}$. It should be noted that the recovery operator only depends on W, J, R , and is independent of the particular image being reconstructed.

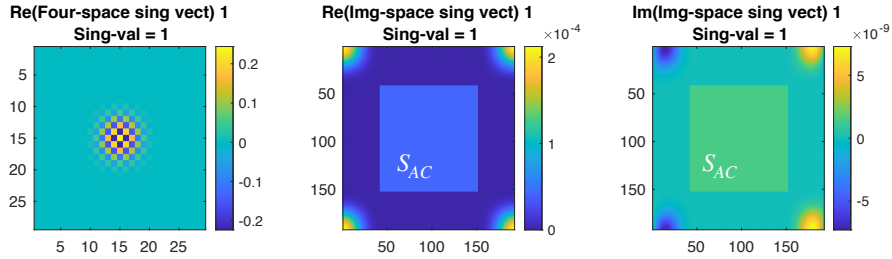


Figure 3: The singular vector \mathbf{u}_1 of $\mathcal{F}_{R,W}^*$, corresponding to the largest singular value 1. On the left is the DFT representation, showing a small neighborhood of W . In the middle is a plot of $\text{Re}(\mathcal{F}^*(\mathbf{u}_1))$ and on the right is a plot of $\text{Im}(\mathcal{F}^*(\mathbf{u}_1))$. The set S_{AC} is indicated in the middle and right panels as a lightly shaded rectangle.

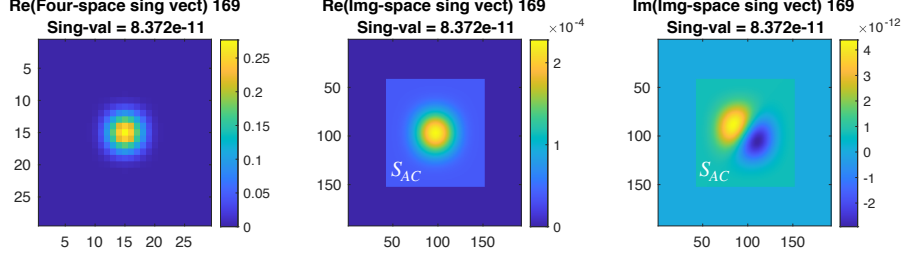


Figure 4: The singular vector \mathbf{u}_{169} of $\mathcal{F}_{R,W}^*$, corresponding to the smallest singular value 9.15×10^{-6} . On the left is the DFT representation, showing a small neighborhood of W . In the middle is a plot of $\text{Re}(\mathcal{F}^*(\mathbf{u}_1))$ and on the right is a plot of $\text{Im}(\mathcal{F}^*(\mathbf{u}_1))$. The set S_{AC} is indicated in the middle and right panels as a lightly shaded rectangle.

Since $\mathcal{F}_{R,W}^*$ is the composition of the unitary map \mathcal{F}^* with orthogonal projections, its singular values lie between 0 and 1. It is straightforward to describe the sorts of images that lead to singular vectors with singular values very close to 1, or very close to 0. In order for $\mathbf{u} \in \mathbb{C}^J$ to satisfy $|\mathcal{F}_{R,W}^* \mathbf{u}| \approx |\mathbf{u}|$, it is necessary for \mathbf{u} to be supported in W and for $\mathcal{F}^*(\mathbf{u})$ to be almost entirely supported in R . An example is shown in Figure 3. The larger R is, the easier it is to find such images.

On the other hand, for $\mathcal{F}_{R,W}^* \mathbf{u} \approx \mathbf{0}$ it is necessary for \mathbf{u} to be supported in W and $\mathcal{F}^*(\mathbf{u})$ to be supported almost entirely in $J \setminus R$. In $2d$, these images resemble tensor products of sampled Hermite functions. For a fixed W , such vectors become more plentiful as R gets smaller. An example is shown in Figure 4. For these examples we use a thrice oversampled 192×192 grid; W is a 13×13 square centered on $\mathbf{k} = (0, 0)$, and $|R| = 24,765$. In most practical examples the largest singular value of $\mathcal{F}_{R,W}^*$ is very close to 1. In this example, the ratio of the largest to smallest singular value of $\mathcal{F}_{R,W}^*$ is 1.0929×10^5 . This quantity represents the conditioning of the problem of recovering the samples of magnitude DFT in W , and is also the norm of $\mathcal{F}_{R,W}^{*\dagger}$. In Section 3 we give estimates and asymptotic results for the conditioning of this problem.

From Fig. 4, we see that the singular vector with the smallest singular value is essentially a Gaussian centered at $\mathbf{0}$. In fact, this vector turns out to provide the most important contribution to “filling the hole” in \mathbf{k} -space. This is easily understood in terms of the continuum model embodied in equations (3) and (4). Since ρ is compactly supported, its Fourier transform is smooth and has a Taylor expansion about zero, $\hat{\rho}(\mathbf{k}) = \hat{\rho}(\mathbf{0}) + \langle \nabla \hat{\rho}(\mathbf{0}), \mathbf{k} \rangle + \frac{1}{2} \langle H_{\hat{\rho}}(\mathbf{0}) \mathbf{k}, \mathbf{k} \rangle + O(\|\mathbf{k}\|^3)$, where $H_{\hat{\rho}}(\mathbf{0})$ is the matrix of second derivatives of $\hat{\rho}$ at $\mathbf{0}$. For ρ a real valued

function this implies that

$$|\hat{\rho}(\mathbf{k})|^2 = |\hat{\rho}(\mathbf{0})|^2 \exp(-\langle B\mathbf{k}, \mathbf{k} \rangle) + O(\|\mathbf{k}\|^4), \quad (13)$$

where

$$\langle B\mathbf{k}, \mathbf{k} \rangle = \frac{1}{|\hat{\rho}(\mathbf{0})|^2} [|\langle \nabla \hat{\rho}(\mathbf{0}), \mathbf{k} \rangle|^2 - \hat{\rho}(\mathbf{0}) \langle H_{\hat{\rho}}(\mathbf{0}) \mathbf{k}, \mathbf{k} \rangle]. \quad (14)$$

For the sort of functions that arise in CDI, the zero Fourier coefficient $\hat{\rho}(\mathbf{0})$ is much larger than any other. The analysis above shows that, near to $\mathbf{k} = \mathbf{0}$, the function $|\hat{\rho}(\mathbf{k})|^2$ strongly resembles a Gaussian, as does the singular vector of $\mathcal{F}_{R,W}^*$ with the smallest singular value. As we see in the next example, this singular vector plays a dominant role in filling in the unmeasured magnitude DFT data.

Example 1. Let $\{\mathbf{v}_l : l = 1, \dots, 169\}$ denote the right singular vectors defined by the matrix $\mathcal{F}_{R,W}^*$ used in Figures 3 and 4, with the corresponding singular values $\{\sigma_l\}$ in decreasing order. The solution to equation (8) can then be represented as

$$\boldsymbol{\alpha}_W = \sum_{l=1}^{169} c_l \mathbf{v}_l. \quad (15)$$

Figure 5[a] shows the coefficient vector \mathbf{c} , defined by a non-negative image similar to those used in Example 2, and Figure 5[b] shows the coefficient vector defined by an image having both signs, but still having a large mean value. From these plots it is quite apparent that c_{169} is nearly an order of magnitude larger than any other coefficient.

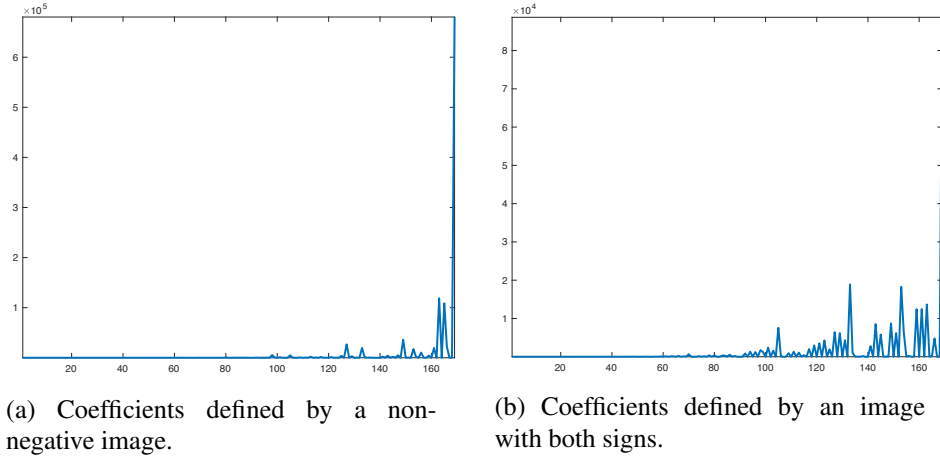


Figure 5: The coefficient vectors from equation (15) defined by real images.

3 The Norm of the Recovery Operator

The recovery operator is defined in (12) as the composition of $\mathcal{F}_{R,W}^{*\dagger}$, the Moore-Penrose inverse of $\mathcal{F}_{R,W}^*$, with \mathcal{F}_{R,W^c}^* . The operator \mathcal{F}_{R,W^c}^* is a composition of orthogonal projections with the unitary operator \mathcal{F}^* , and therefore its norm is bounded by 1. Let $\sigma_1 \geq \sigma_2 \geq \dots \geq \sigma_{|W|}$ denote the singular values of $\mathcal{F}_{R,W}^*$ in decreasing order. The norm of $\mathcal{R}_{R,W}$ is therefore bounded above by $\sigma_{|W|}^{-1}$, but, in fact, may be smaller.

In this section, we restrict our attention to the case that W is a square subregion of J and R is the *complement* of the rectangular subregion $S_{AC} = S \ominus S$ within the field of view. Over the years, a great deal of effort has been expended to understand the singular values of operators like $\mathcal{F}_{S_{AC},W}^*$, a field of research that goes, at least in continuum case, under the rubric of “prolate spheroidal functions,” see [21, 20, 13]. Because \mathcal{F}^* is a unitary map, and $R = S_{AC}^c$, it follows that

$$\|\alpha_W\|^2 = \|\mathcal{F}_{R,W}^* \alpha_W\|^2 + \|\mathcal{F}_{S_{AC},W}^* \alpha_W\|^2, \quad (16)$$

and therefore:

$$\mu_0(R, W, d) = \sigma_{|W|}^2 = \min_{\alpha_W \neq 0} \frac{\|\mathcal{F}_{R,W}^* \alpha_W\|^2}{\|\alpha_W\|^2} = 1 - \max_{\alpha_W \neq 0} \frac{\|\mathcal{F}_{S_{AC},W}^* \alpha_W\|^2}{\|\alpha_W\|^2}. \quad (17)$$

That is, there is a simple relationship between the smallest singular value of $\mathcal{F}_{R,W}^*$ and the largest singular value of $\mathcal{F}_{S_{AC},W}^*$. In fact this is a special case of the following theorem:

Theorem 2. *Let $K, L \subset J$ and assume that $|K| \leq |L|$. We let $\{\sigma_j\}$ denote the singular values of $\mathcal{F}_{L,K}^*$ in decreasing order and $\{\tau_j\}$ the singular values of $\mathcal{F}_{L^c,K}^*$, also in decreasing order. If $p = |K|$, then, for $1 \leq j \leq p$,*

$$\sigma_j^2 = 1 - \tau_{p-j+1}^2. \quad (18)$$

Note that K, L are arbitrary subsets of J subject to the requirement that $|K| \leq |L|$. The proof of the theorem is given in Appendix B.

This theorem is very useful in the present setting, where W is a rectangular region and R the complement of a rectangular region: it allows us to reduce the analysis of the singular values of $\mathcal{F}_{R,W}^*$, to the case of $\mathcal{F}_{S_{AC},W}^*$. Recalling that $w = \lfloor 1 + mk_0 \rfloor$, with $W = [1 - w : w - 1]^d$ and $S_{AC} = [-\beta N : \beta N]^d$, we let $\{\tau_{j,d}\}$ be the singular values of $\mathcal{F}_{S_{AC},W}^*$, in the d -dimensional case, and $\{\sigma_{j,d}\}$, the singular values of $\mathcal{F}_{R,W}^*$. Because the d -dimensional DFT is the d -fold tensor product of 1-dimensional transforms, it is not difficult to show that

$$\tau_{1,d} = \tau_{1,1}^d. \quad (19)$$

If $q = |W|$, then Theorem 2 implies that

$$\sigma_{q,d} = \sqrt{1 - \tau_{1,d}^2}.$$

As follows from the analysis in Appendix A, $\tau_{1,1}^2 = (1 - \epsilon)$, for an $\epsilon \ll 1$, which implies that

$$\tau_{1,d}^2 = (1 - \epsilon)^d = 1 - d\epsilon + O(\epsilon^2), \quad (20)$$

and therefore

$$\sigma_{q,d} = \sqrt{1 - \tau_{1,d}^2} \approx \sqrt{1 - (1 - d\epsilon)} \approx \sqrt{d\epsilon}. \quad (21)$$

The norm of the operator of interest in the hole-filling-problem is given approximately by:

$$[\mu_0(S_{AC}, W, d)]^{-\frac{1}{2}} = \sigma_{q,d}^{-1} \approx \frac{1}{\sqrt{d\epsilon}}. \quad (22)$$

In Appendix A we show how to get an asymptotic estimate for the quantity $\mu_0(S_{AC}, W, 1)$, which depends only the “space-bandwidth” product, βk_0 . Asymptotically, as $\beta k_0, m, N \rightarrow \infty$, we show that

$$\epsilon = \mu_0(S_{AC}, W, 1) \sim 4\pi\sqrt{\beta k_0}e^{-2\pi\beta k_0}. \quad (23)$$

This formula, along with (22) imply the asymptotic formula:

$$\|\mathcal{R}_{W,R}\| \sim \frac{e^{\pi\beta k_0}}{\sqrt{4\pi d}[\beta k_0]^{\frac{1}{4}}}. \quad (24)$$

Note that the exponent in (24) does not depend on the dimension.

The recent analysis in [3] gives a lower bound, which is slightly different, indicating that increased sampling, and oversampling might have the effect of slightly decreasing the norm of $\mathcal{R}_{W,R}$. A result of Slepian (reproduced in [3]) shows, that as $m \rightarrow \infty$,

$$\|\mathcal{R}_{W,R}\| \sim \frac{C_{k_0,m,N}}{\sqrt{d}} \left[\frac{1 + \tan\left(\frac{\pi\beta}{4m}\right)}{1 - \tan\left(\frac{\pi\beta}{4m}\right)} \right]^{2mk_0+1}, \quad (25)$$

see [20]. Here $C_{k_0,m,N}$ is an algebraic factor. As $m \rightarrow \infty$ this formula gives the same exponential rate as (24).

It is worth noting that the exponential rate in the conditioning of the hole-filling problem does *not* depend on the dimension. In fact the condition number should decrease, albeit slowly, as the dimension increases. The computations in Example 3 show that (24) is fairly accurate, even for moderate values of βk_0 , N , and $m \geq 3$. The main lessons of this analysis are:

1. The size of the hole in \mathbf{k} -space that can be stably filled using the linear method we have introduced depends mostly on the product βk_0 .
2. The norm of recovery operator grows exponentially with this product. Recalling that $1 < \beta < 2$, the size of the hole, as measured by k_0 , that can be filled in this way is quite limited. However, the exponential rate does *not* depend on the dimension!

In the examples in the next section we see that, for a given β and k_0 , larger values of m do provide a better result, though with little improvement beyond $m = 4$.

4 Examples

We now consider several examples that illustrate the performance of this method on $2d$ -images, and the dependence of $\|\mathcal{R}_{W,R}\|$ on m, N, k_0 , and β . It should be recalled that oversampling is a matter of changing the spacing between the samples collected in \mathbf{k} -space, and not the maximum frequency collected. As follows from (4), the double-oversampled Fourier coefficient with indices $(2k_1, 2k_2)$ is at the same spatial frequency as the triple-oversampled coefficient with indices $(3k_1, 3k_2)$.

Example 2. For these examples we use an image, ρ , taking both signs that sits in a 64×64 -rectangle. The function sampled is twice differentiable; for the estimate of the support S , we use the 1-pixel neighborhood of the smallest rectangle that contains $\text{supp } \rho$. We use either double, $|J| = 128 \times 128$, or triple, $|J| = 192 \times 192$, oversampling, and remove neighborhoods, W , of $\mathbf{0}$ in \mathbf{k} -space of various sizes. In all cases we solve for the missing values using (11).

Figure 6 shows the results with double oversampling and Figure 7, the results with triple oversampling. The plots in the upper left corners show the singular values, in decreasing order, of $\mathcal{F}_{R,W}^*$. The plots in the upper right corners show the set R in yellow. The support of ρ is contained in the union of the light blue and dark blue rectangles and the hole in \mathbf{k} -space is dark blue. The plots in the lower left corners are the recovered magnitude-DFT coefficients in W of the autocorrelation function, using the values found in (11) to “fill the hole.” The errors in the autocorrelation images are shown in the lower right corners.

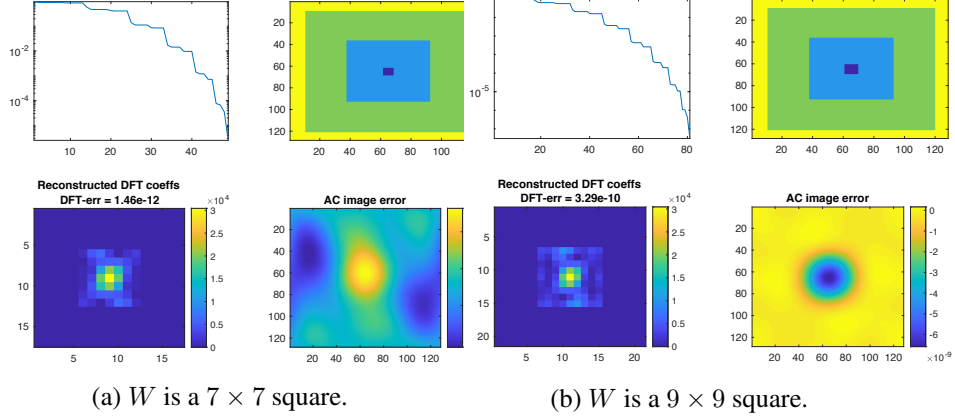


Figure 6: Plots connected with the recovery of missing samples of the magnitude DFT data using double-oversampling.

With triple oversampling we can recover the data with 11 digits of accuracy in a fairly large hole (15×15 -hole in a 192×192 grid), and the matrix $\mathcal{F}_{R,W}^*$ has most of its singular values close to 1. With double oversampling the conditioning of the matrix $\mathcal{F}_{R,W}^*$ deteriorates more quickly.

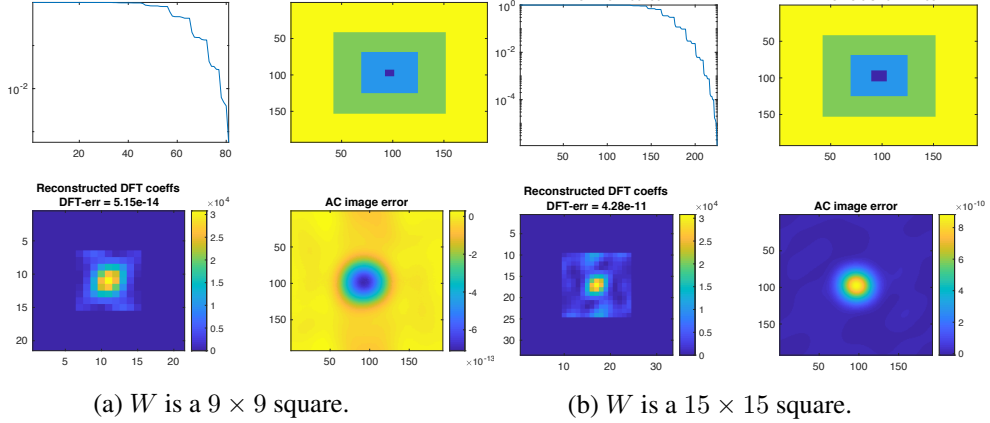


Figure 7: Plots connected with the recovery of missing samples of the magnitude DFT data using triple-oversampling.

We now make a systematic study of the dependence of $\|\mathcal{R}_{R,W}\|$ on the various parameters that define this operator: m , the degree of oversampling, N , the “base” number of samples, k_0 the maximum spatial frequency not sampled. For these examples we fix $\beta = 1.5$, so that the autocorrelation image is supported in

$[-1.5N : 1.5N]^2$. As predicted from the asymptotic formula, (24), the norm of $\mathcal{R}_{R,W}$ increases monotonically with β .

Example 3. In these examples the images are indexed by $J = [1 - mN : mN]^2$, the image itself is supported in a proper subset of $[-N : N]^2$, its autocorrelation image is supported in $[-1.5N, 1.5N]^2$, and samples of the magnitude DFT with indices in $[1 - w : w - 1]^2$, are *not* measured. As before, $w = \lfloor 1 + mk_0 \rfloor$.

The asymptotic formula in (24) is expected to become increasingly accurate as m, N grow. In fact, taking $N = 128$, and $m = 3$ already leads to fairly good agreement with this estimate. To generate the tables below we fix $\beta = 1.5$ and consider various values of m, k_0 for $N = 64, 128, 256$. Taking $m = 3$ results in a large improvement over taking $m = 2$, but $m = 4$ only provides a small improvement over $m = 3$.

$N = 64$	$m = 2$	$m = 3$	$m = 4$	Asymp. Val.
$k_0 = 1$	337.8	70.87	45.4	20.06
$k_0 = 2$	1.73×10^5	1.12×10^4	5.42×10^3	1.88×10^3
$k_0 = 3$	1.08×10^8	1.99×10^6	7.25×10^5	1.89×10^5
$k_0 = 4$	8.61×10^{10}	3.89×10^8	1.05×10^8	1.96×10^7
$k_0 = 5$	9.52×10^{13}	8.44×10^{10}	1.65×10^{10}	2.06×10^9

Table 1: Values of $\|\mathcal{R}_{R,W}\|$ for $\beta = 1.5$, $N = 64$ and various choices of m, k_0 . The asymptotic values predicted by (24) are shown in the last column.

The following tables are generated with $N = 128$, and $N = 256$. The values in this table that overlap with those in Table 1 are quite similar, with generally smaller values than for $N = 64$.

$N = 128$	$m = 2$	$m = 3$	$m = 4$	Asymp. Val.
$k_0 = 1$	361.03	73.31	46.7	20.06
$k_0 = 2$	1.843×10^5	1.17×10^4	5.67×10^3	1.88×10^3
$k_0 = 3$	1.05×10^8	2.05×10^6	7.52×10^5	1.89×10^5
$k_0 = 4$	6.45×10^{10}	3.77×10^8	1.04×10^8	1.96×10^7
$N = 256$	$m = 2$	$m = 3$	$m = 4$	Asymp. Val.
$k_0 = 1$	373.17	74.63	47.4	20.06
$k_0 = 2$	1.94×10^5	1.21×10^4	5.81×10^3	1.88×10^3
$k_0 = 3$	1.09×10^8	2.13×10^6	7.76×10^5	1.89×10^5
$k_0 = 4$	6.45×10^{10}	3.88×10^8	2.96×10^7	1.96×10^7

Table 2: Values of $\|\mathcal{R}_{R,W}\|$ for $\beta = 1.5$, $N = 128, 256$ and various choices of m, k_0 . The asymptotic values predicted by (24) are shown in the last column.

To close this section we consider the relationship in the errors of the recovered DFT magnitude data, versus that in the squared magnitude data. We express the

recovered autocorrelation magnitude data, $\{u_{\mathbf{k}}^2 : \mathbf{k} \in W\}$, as

$$u_{\mathbf{k}}^2 = |\hat{\rho}_{\mathbf{k}}|^2 + \epsilon_{\mathbf{k}}, \text{ so that } \frac{|u_{\mathbf{k}}^2 - |\hat{\rho}_{\mathbf{k}}|^2|}{|\hat{\rho}_{\mathbf{k}}|^2} = \frac{\epsilon_{\mathbf{k}}}{|\hat{\rho}_{\mathbf{k}}|^2}. \quad (26)$$

Clearly we have that

$$u_{\mathbf{k}} \approx |\hat{\rho}_{\mathbf{k}}| + \frac{\epsilon_{\mathbf{k}}}{2|\hat{\rho}_{\mathbf{k}}|}, \quad (27)$$

and therefore

$$\frac{||\hat{\rho}_{\mathbf{k}}| - u_{\mathbf{k}}|}{|\hat{\rho}_{\mathbf{k}}|} \approx \frac{\epsilon_{\mathbf{k}}}{2|\hat{\rho}_{\mathbf{k}}|^2}. \quad (28)$$

For \mathbf{k} near to zero, the magnitude DFT coefficients, $|\hat{\rho}_{\mathbf{k}}|$, tend to be large, and therefore we can expect these recovered values to have somewhat smaller relative errors than their squared counterparts. This, however, does not mean that the relative mean square error is smaller for $|\hat{\rho}_{\mathbf{k}}|$ than for $|\hat{\rho}_{\mathbf{k}}|^2$. An example comparing these errors is shown in Figure 8. This resulted from filling a 13×13 -hole for a thrice oversampled 64×64 -image. The data used here is noise-free.

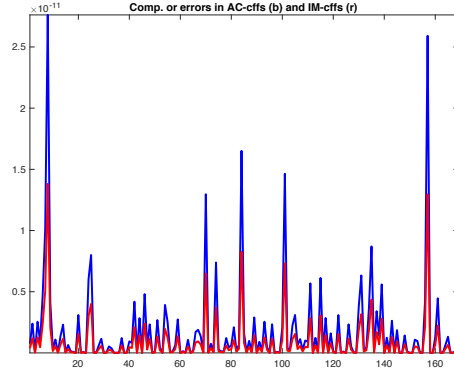


Figure 8: Relative errors in recovery of $\{|\hat{\rho}_{\mathbf{k}}|^2\}$ (blue curve) versus those for recovered values of $\{|\hat{\rho}_{\mathbf{k}}|\}$ (red curve).

5 The Effects of Noise

We now consider the effects of noise on the recovery process. Let $\mathbf{n} \in \mathbb{R}^{W^c}$ represent the measurement error and noise. Then, instead of solving (8), we actually need to solve the equation

$$\mathcal{F}_{R,W}^*(\alpha_0 + \beta) = -\mathcal{F}_{R,W^c}^*(\mathbf{a} + \mathbf{n}). \quad (29)$$

The relative effect of the noise introduced into α_0 is then measured by the ratio

$$\frac{\|\beta\|}{\|\mathbf{n}\|} = \frac{\|\mathcal{R}_{R,W}\mathbf{n}\|}{\|\mathbf{n}\|}. \quad (30)$$

The matrix $\mathcal{R}_{R,W}$ has a representation of the form

$$\mathcal{R}_{R,W} = \sum_{j=1}^{|W|} \nu_j \mathbf{w}_j \otimes \mathbf{z}_j^*, \quad (31)$$

where $\{\mathbf{w}_j : j = 1, \dots, |W|\}$ is an orthonormal basis for the range and $\{\mathbf{z}_j : j = 1, \dots, |W|\}$, are pairwise orthonormal. For a vector \mathbf{n}

$$\|\mathcal{R}_{R,W}\mathbf{n}\|^2 = \sum_{j=1}^{|W|} \nu_j^2 |\langle \mathbf{n}, \mathbf{z}_j \rangle|^2. \quad (32)$$

The collection of vectors $\{\mathbf{z}_j\}$ can be augmented to give an orthonormal basis, $\{\mathbf{z}_j : j = 1, \dots, |W^c|\}$, for \mathbb{R}^{W^c} . Hence for $\mathbf{n} \in \mathbb{R}^{W^c}$, we have that

$$\sum_{j=1}^{|W^c|} |\langle \mathbf{n}, \mathbf{z}_j \rangle|^2 = \|\mathbf{n}\|^2. \quad (33)$$

It is often reasonable to assume that the random variables $\{|\langle \mathbf{n}, \mathbf{z}_j \rangle|^2 : j = 1, \dots, |W^c|\}$ are independent and identically distributed, and therefore the expected values satisfy:

$$\mathbb{E}(|\langle \mathbf{n}, \mathbf{z}_j \rangle|^2) = \frac{\|\mathbf{n}\|^2}{|W^c|}. \quad (34)$$

This would be the case for any additive, I.I.D. noise process. In this case

$$\mathbb{E}\left(\frac{\|\mathcal{R}_{R,W}\mathbf{n}\|^2}{\|\mathbf{n}\|^2}\right) = \frac{1}{|W^c|} \left[\sum_{j=1}^{|W|} \nu_j^2 \right]. \quad (35)$$

From the Cauchy-Schwarz inequality it follows that

$$\mathbb{E}\left(\frac{\|\mathcal{R}_{R,W}\mathbf{n}\|}{\|\mathbf{n}\|}\right) \leq \frac{1}{\sqrt{|W^c|}} \left[\sum_{j=1}^{|W|} \nu_j^2 \right]^{\frac{1}{2}}. \quad (36)$$

Even when the norm of $\mathcal{R}_{R,W}$ is large, the quantity appearing on the right hand side of (36) may turn out to be rather modest. This value gives a good estimate for

the effect of noise on the accuracy of the recovered values of the unmeasured DFT modulus data. The number $\sqrt{|W^c|} \approx mN$, (in $2d$), which shows that a potential advantage of greater oversampling is better noise suppression when recovering the unmeasured DFT magnitude data.

As is well known, an important source of noise in CDI applications is Poisson noise that arises from the discreteness of X-ray photons. This is usually modeled as follows: if $|\hat{\rho}_{\mathbf{k}}|^2$ is the “true intensity” of the DFT coefficient in the \mathbf{k} th pixel, then measurement $\tilde{a}_{\mathbf{k}}^2$ is a sample of a Poisson random variable with intensity $|\hat{\rho}_{\mathbf{k}}|^2$. The “noise” in this pixel is therefore given by

$$n_{\mathbf{k}} = \tilde{a}_{\mathbf{k}}^2 - |\hat{\rho}_{\mathbf{k}}|^2. \quad (37)$$

Clearly $\mathbb{E}(n_{\mathbf{k}}) = 0$, and $\mathbb{E}(n_{\mathbf{k}}^2) = |\hat{\rho}_{\mathbf{k}}|^2$, and therefore the SNR is $|\hat{\rho}_{\mathbf{k}}|$, which implies that the Poisson noise process has a pixel dependent SNR. As $\mathbb{E}(n_{\mathbf{k}}^2) = \mathbb{E}(\tilde{a}_{\mathbf{k}}^2)$, the noise is in some ways similar to the image itself. Indeed, the projection of $\mathcal{F}_{R,W^c}^* \mathbf{n}$ into the range of $\mathcal{F}_{R,W}^*$ tends to be rather large.

Figure 9 shows histograms of the ratios, $\frac{\|\mathcal{R}_{R,W} \mathbf{n}\|}{\|\mathbf{n}\|}$, for different noise processes in a triple oversampled example, where the condition number of $\mathcal{R}_{R,W}$ is 1.093×10^5 . These ratios are typically less than 400, for uniform and Gaussian noise, and less than 2000, for Poisson noise. The much smaller numbers in Gaussian and uniform cases are a reflection of the fact that the orthogonal projection of $\mathcal{F}_{R,W^c}^* \mathbf{n}$ into the range of $\mathcal{F}_{R,W}^*$ tends to be quite small for \mathbf{n} a sample of an additive I.I.D. noise process, as predicted in (36). As suggested by the discussion above, the situation is rather different in the Poisson case.

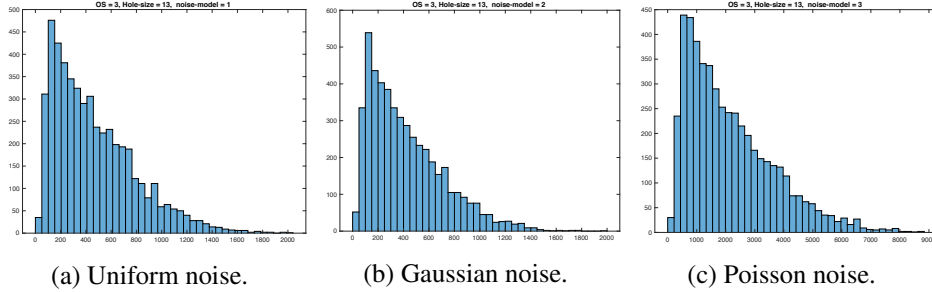


Figure 9: Histograms of the ratios $\|\mathcal{R}_{R,W} \mathbf{n}\| / \|\mathbf{n}\|$ for 5000 trials of uniform, Gaussian and Poisson noise. Here $w = 7, m = 3, N = 64$.

6 Hole Filling and Image Reconstruction

In this final section we consider how the hole-filling procedure outlined above affects the outcome of image reconstruction using an HIO-algorithm, see [12, 5]. This algorithm, which iterates a map like that in (38), is currently the basis for the best known, and most frequently used phase retrieval method. In the examples in this section we see that, for a certain range of hole-sizes and in the absence of noise, the images obtained by first filling in the unmeasured data using equation (11), and then using HIO are much better than those obtained by simply using HIO. The picture is more complicated when there is noise, with the results now depending on the character of the noise and the SNR. With noise, we find that it is often useful to use some of the values recovered using equation (11), and allow others to be filled in implicitly using HIO.

Suppose the data is of the form given by (6), where α_{W^c} denotes the measurements outside of the missing hole W . Let P_A denote the projection operator onto the nearest point in some set A . We set $B_S = \{\rho : P_{S^c}(\rho) = 0\}$ and $\mathbb{A}_a = \{\rho : |P_{W^c} \circ \mathcal{F}(\rho)|^2 = \alpha_{W^c}\}$. HIO and related algorithms provide an update of the form:

$$\rho^{(k+1)} = \rho^{(k)} + P_{\mathbb{A}_a} \circ R_{B_S}(\rho^{(k)}) - P_{B_S}(\rho^{(k)}), \quad (38)$$

where $R_{B_S}(\rho) = 2P_{B_S}(\rho) - \rho$.

Note that (38) operates agnostically in regards to the missing data inside W , for every missing data value one less constraint equation is imposed. Thus, conceivably filling in the missing data in W before applying HIO (or any such phase retrieval algorithm) could improve the quality of the reconstructed image.

Extensive numerical simulations indeed confirm this to be true. We fix a test image and the set of corresponding squared DFT magnitude measurements, $\alpha_{W^c}^2$, with low frequencies removed that belong to a square, W , of size $(2w-1) \times (2w-1)$ centered on $(0,0)$. Here, we use triple oversampling so that $w = \lfloor *1 + 3k_0 \rfloor$. We then compare the following two recovery procedures: (i) HIO is directly applied to the “measured” data $\alpha_{W^c}^2$, and (ii) the missing data in W is first filled in using the recovery operator, and then HIO is applied to the full data set α^2 (henceforth referred to as the “Fill+HIO” algorithm). It is observed that Fill+HIO produces superior image reconstruction for values of k_0 for which the linear system, given by (8), can be solved accurately. Fill+HIO provides improved recovery up to $w = 15$ ($k_0 \approx 5$), whereas HIO alone fails after $w = 6$ ($k_0 \approx 2$). Typical comparative results on simulated CDI data are shown in Figs 10 and 11.

Practical approaches for the phase retrieval problem in the presence of noisy data typically involve numerical optimization [19, 1] and data-driven methods,

see [16], topics that are outside the scope of this paper and which we do not pursue further. However, we do provide some general remarks, and guidelines for applying the Fill+HIO algorithm to problems with noisy data.

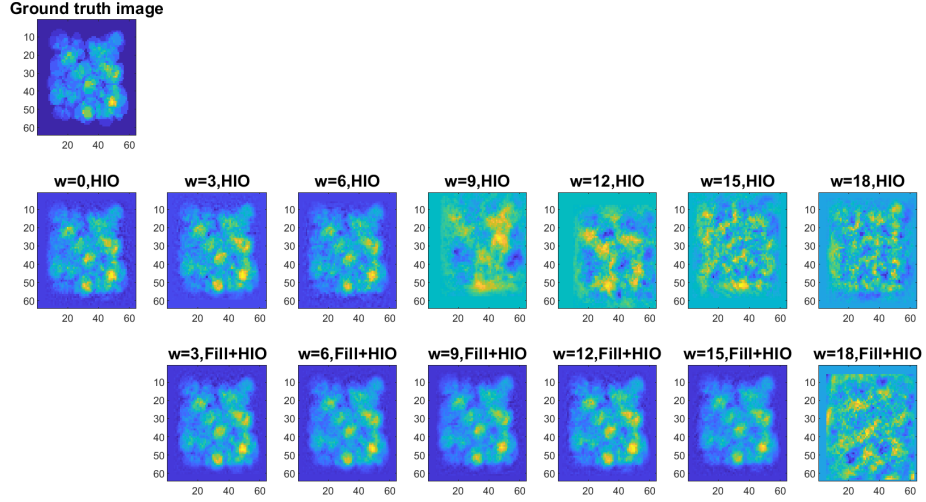


Figure 10: Image reconstruction via HIO alone, in the middle row, versus phase retrieval using hole-filling followed by HIO (“Fill+HIO”) in the bottom row. The image is of size 64×64 , and data is of size 192×192 , so $m = 3$, and the $(2w - 1) \times (2w - 1)$ frequencies centered on $(0, 0)$ zeroed-out.

When used with real measurements, the filled-in data values obtained via (11) are necessarily contaminated by noise. Thus, there arises a tradeoff between ignoring the missing data and first recovering estimates for these values which contain errors. It is observed from numerical simulations that, with noisy data, the best image reconstruction is achieved by utilizing a subset of the data found using (11), and allowing HIO to recover the remaining coefficients.

A natural procedure for determining the best subset to choose is to run multiple trials of the Fill+HIO procedure where, for each trial, the amount of recovered data that is used is incrementally increased. While, in practice, the true smallest error achieved throughout such trials is unknown (since the ground-truth image is unknown), an empirically successful proxy is to consider the *data error* for each trial; if ρ is the approximate reconstruction satisfying the support condition, then

the data error is:

$$\frac{\left\| |\widehat{\rho}|^2 - |\widehat{\rho}_0|^2 \right\|_2}{\left\| |\widehat{\rho}_0|^2 \right\|_2}. \quad (39)$$

For our experiments we choose the partial filling that minimizes this quantity.

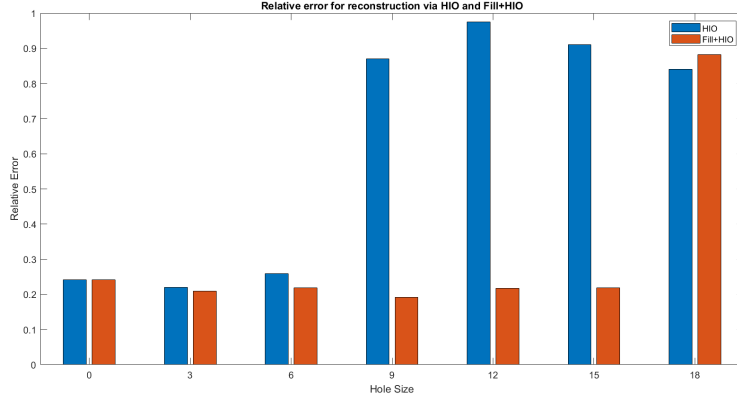


Figure 11: Relative errors $\frac{\|\rho - \rho_0\|_2}{\|\rho_0\|_2}$ for the ground truth image ρ_0 shown in Fig. 1 and the recovered images ρ using the HIO (blue) and Fill+HIO (orange) algorithms, respectively. Data has the $(2w-1) \times (2w-1)$ square of lowest frequencies zeroed-out.

We concentrate on the case of data corrupted by Poisson noise, such as typically occurs in CDI experiments. The discussion at the end of Section 2 clearly indicates that the largest amplification of noise occurs in the recovery of the lowest-frequency values. Thus, a natural search strategy for partially filling a rectangle of missing data with recovered values is to work from the outer boundary of W inward, considering annular regions, which restore the mid-range of missing frequencies.

We apply this procedure to simulated CDI data, corresponding to the setup in Figs. 10 and 11, when $w = 5, m = 3$, that is corrupted by Poisson noise with a signal-to-noise ratio of 1000. Over 1000 trials, we observe that the distribution of the recovery error is noticeably improved by restoring some of the missing data before running HIO. This is illustrated in the histograms shown in Figure 12.

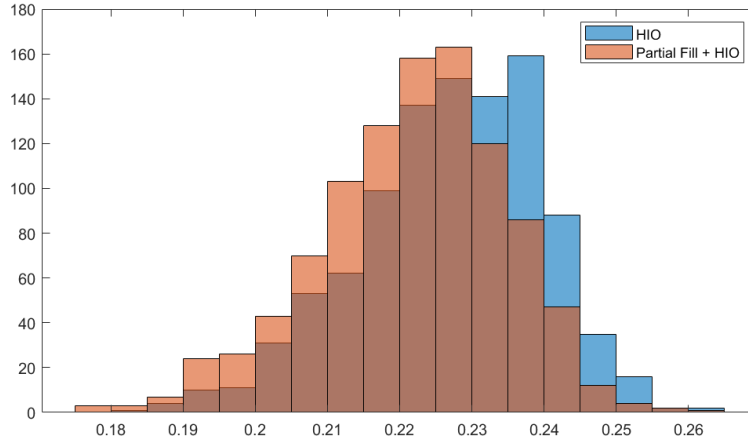


Figure 12: Histograms of relative error values generated from 1000 noisy instances of the simulated CDI setup shown in Figure 10, using the HIO (blue) and Partial Fill+HIO (orange) algorithms, respectively. Partial Fill+HIO significantly improves the error distribution.

7 Conclusions

In this paper, we have investigated the problem of recovering the unmeasured data within the beamstop in CDI imaging. Rather than including the full complex Fourier transform at these missing locations as part of a global inverse problem, we have shown that the modulus Fourier data within the beamstop can itself be recovered, as the solution to a linear least squares problem. Algorithms for phase retrieval can then be used in a second step on this “filled in” data set. The power of this approach is illustrated in Fig. 11.

We also analyzed under what conditions this method of recovery is likely to be successful. If W and S_{AC} are rectangular subsets of J , then the answer hinges on the value of the dimensionless parameter βk_0 , here $\beta > 1$ is determined by the support of the autocorrelation function $\rho \star \rho$, and $2k_0$ is the hole width. In this analysis, we assume the object of interest has spatial dimensions normalized to unit length.

Our analysis provides a generalization of Hayes’ theorem [14] to the case of phase retrieval with missing data. Theorem 1, shows that, very often, the missing data, hidden by the beamstop, can be *uniquely* recovered from the measured magnitude data. Hayes’ theorem then applies directly to the completed data set to show that the solution to the phase retrieval problem is again generically unique.

This method for recovering the unmeasured magnitude data should be applicable to many classical phase retrieval problems. We are currently investigating the extension of our results to other X-ray imaging modalities.

A Appendix

In this appendix we derive an asymptotic bound for $\mu_0(R, W, d)$, assuming that W and $S_{AC} = R^c$ are rectangular subsets. This bound becomes more accurate as m, N tend to infinity and the product βk_0 grows. A similar question is addressed in Barnett's recent paper [3] on the conditioning of sub-blocks of the DFT matrix. An upper bound on $\mu_0(R, W, 1)$, follows from the estimates in Barnett's paper.

In (17) we show that

$$\mu_0(S_{AC}, W, d) = 1 - \max_{\alpha_W \neq 0} \frac{\|\mathcal{F}_{S_{AC}, W}^* \alpha_W\|^2}{\|\alpha_W\|^2}. \quad (40)$$

It should first be noted that as $\mathcal{F}^* \alpha = [\mathcal{F}(\overline{\alpha})]^*$, replacing \mathcal{F}^* with \mathcal{F} does not change the value of the maximum in this formula. The key consequence of this formula is that the smallest singular value of $\mathcal{F}_{R, W}^*$ is determined by the largest singular value of $\mathcal{F}_{S_{AC}, W}^*$. Because $S_{AC} \subset J$ is a rectangular set, and the d -dimensional DFT is a tensor product of 1-dimensional DFTs, this allows the determination of these singular values as products of singular values that arise in the 1-dimensional case.

With this in mind, we let α be a sequence of length $2mN$ supported in $[1 - w : w - 1]$, and f , a real valued function supported in $[-k_0, k_0]$, where $w = \lfloor 1 + mk_0 \rfloor$, with $f\left(\frac{j}{m}\right) = \sqrt{\frac{m}{2N}} \alpha_j$. The discrete Fourier transform of α is

$$\hat{\alpha}_k = \frac{1}{m} \sum_{j=-w}^w f\left(\frac{j}{m}\right) e^{-\frac{2\pi i j k}{2mN}} \approx \hat{f}\left(\frac{k}{2N}\right). \quad (41)$$

With these approximations it follows that

$$\begin{aligned} \sum_{k=-\beta N}^{\beta N} |\hat{\alpha}_k|^2 &\approx \sum_{k=-\beta N}^{\beta N} \left| \hat{f}\left(\frac{k}{2N}\right) \right|^2, \\ \sum_{j=1-w}^{w-1} |\alpha_j|^2 &\approx 2N \int_{-k_0}^{k_0} |f(x)|^2 dx, \end{aligned} \quad (42)$$

and therefore the ratio, whose maximum defines $\mu_0([-\beta N : \beta N], [1 - w : w - 1], 1)$, is approximated by:

$$\frac{\sum_{k=-\beta N}^{\beta N} |\hat{\alpha}_k|^2}{\sum_{j=1-w}^{w-1} |\alpha_j|^2} \approx \frac{\int_{-\frac{\beta}{2}}^{\frac{\beta}{2}} |\hat{f}(y)|^2 dy}{\int_{-k_0}^{k_0} |f(x)|^2 dx}. \quad (43)$$

As noted above, α is a sequence supported in $[1 - w : w - 1]$. The ratio of the sums on the left hand side converge to the ratio of integrals on the right hand side as $N, m \rightarrow \infty$.

We define

$$\lambda_0(k_0, \beta, 1) = \max_{f \in \mathcal{A}_{k_0}^2 \setminus \{0\}} \left[\frac{\int_{-\frac{\beta}{2}}^{\frac{\beta}{2}} |\hat{f}(y)|^2 dy}{\int_{-k_0}^{k_0} |f(x)|^2 dx} \right], \quad (44)$$

where $\mathcal{A}_{k_0}^2$ consists of functions in $L^2(\mathbb{R})$ supported in $[-k_0, k_0]$. The calculations above show that, at least asymptotically, as m, N grow,

$$\mu_0(S_{AC}, W, 1) \approx 1 - \lambda_0(k_0, \beta, 1). \quad (45)$$

The quantity on the right hand side of (45) has been intensively studied in the literature on prolate spheroidal functions, see [13, 20]; adapting the result of Theorem 1 from [13] we obtain:

$$\mu_0(S_{AC}, W, 12) \sim 4\pi \sqrt{\beta k_0} e^{-2\pi\beta k_0}. \quad (46)$$

The asymptotic evaluation on the right hand side of (46) is in the limit $\beta k_0 \rightarrow \infty$.

In d dimensions, suppose that the support of the autocorrelation image is contained in the cuboid $[-\frac{\beta}{2}, \frac{\beta}{2}]^d$ and $W = [1 - w : w - 1]^d$. Let $\lambda_0(k_0, \beta, d)$ be the d -dimensional analogue of $\lambda_0(k_0, \beta, 1)$; the extremizer defining $\lambda_0(k_0, \beta, d)$, is just the d -fold tensor product of the 1d-extremizer. Hence we see that

$$\begin{aligned} \lambda_0(k_0, \beta, d) &= \lambda_0(k_0, \beta, 1)^d \sim (1 - 4\pi \sqrt{\beta k_0} e^{-2\pi\beta k_0})^d \\ &\approx 1 - 4d\pi \sqrt{\beta k_0} e^{-2\pi\beta k_0}, \end{aligned} \quad (47)$$

and therefore

$$\mu_0(S_{AC}, W, d) \sim 4d\pi \sqrt{\beta k_0} e^{-2\pi\beta k_0}. \quad (48)$$

The norm of $\mathcal{R}_{R,W}$ might be smaller than $[\mu_0(R, W, d)]^{-\frac{1}{2}}$, as \mathcal{F}_{R,W^c}^* has norm less than 1. In fact, in our applications, the norm of \mathcal{F}_{R,W^c}^* is very close to 1. Hence the norm of the recovery operator is given asymptotically by the quantity

$$[\mu_0(S_{AC}, W, d)]^{-\frac{1}{2}} \sim \frac{e^{\pi\beta k_0}}{\sqrt{4d\pi} [\beta k_0]^{\frac{1}{4}}}. \quad (49)$$

Since the minimum singular value of $\mathcal{R}_{R,W}$ is very close to 1, this is also an asymptotic estimate for the condition number.

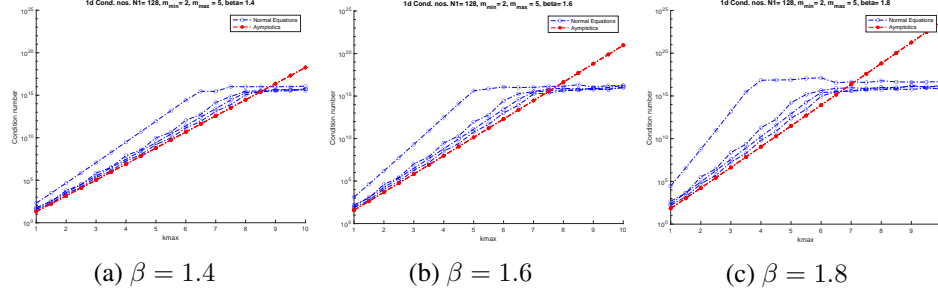


Figure 13: Plots of $[\mu_0(S_{AC}, W, 1)]^{-\frac{1}{2}}$, for $m = 2, 3, 4, 5$, (in blue) along with a plot of the asymptotic formula (in red). In these plots k_0 ranges from 1 to 10, and y -axis goes from 10^0 to 10^{25} .

In Figure 13[a,b,c] we show values of $[\mu_0(S_{AC}, W, 1)]^{-\frac{1}{2}}$, for $\beta = 1.4, 1.6, 1.8$. In each plot, there are 4 blue curves corresponding to $m = 2, 3, 4, 5$, along with the predictions (in red) made by (49), with $d = 1$. The x -axis is k_0 , which ranges from 1 to 10. As m increases, the blue curves get closer to the plot of the asymptotic formula. As long as there is sufficient accuracy in the double precision calculation, the asymptotic formula is close to exact calculation by the time $m = 3$, and is a lower bound throughout this range of parameters. Once the condition number reaches $\sim 10^{15}$, the calculation of $[\mu_0(S_{AC}, W, 1)]^{-\frac{1}{2}}$ saturates and is no longer meaningful. In these computations $N = 128$, and increasing it does not significantly change these results.

This analysis shows that, asymptotically, the size of the hole in k -space that can be stably filled depends mostly on the product βk_0 ; in particular, it does not depend strongly on the extent of oversampling, provided that $m \geq 3$. Perhaps most surprisingly, the norm of $\mathcal{R}_{R,W}$ decreases with the dimension! Figure 13 and the tables in Example 3 show that the asymptotic formula provides a lower bound on $\|\mathcal{R}_{R,W}\|$, which improves as m, N increase.

B Appendix

To prove Theorem 2 we recall the variational characterizations of the singular values of a linear map $A : \mathbb{C}^p \rightarrow \mathbb{C}^n$ and assume that $p \leq n$. It turns out to be simpler in the proof to list the singular values in increasing order: $s_1 \leq s_2 \leq \dots \leq s_p$. Note that if $p > n$, then $s_1 = 0$, which is not too interesting. The j th singular

value of A has 2 variational characterizations:

$$\begin{aligned} s_j^2 &= \min_{\{S \subset \mathbb{C}^p: \dim S=j\}} \max_{\mathbf{x} \in S: \mathbf{x} \neq \mathbf{0}} \frac{\|A\mathbf{x}\|^2}{\|\mathbf{x}\|^2} \\ s_j^2 &= \max_{\{S \subset \mathbb{C}^p: \dim S=p-j+1\}} \min_{\mathbf{x} \in S: \mathbf{x} \neq \mathbf{0}} \frac{\|A\mathbf{x}\|^2}{\|\mathbf{x}\|^2}. \end{aligned} \quad (50)$$

Proof. The basic observation is that, because \mathcal{F} is a unitary map, for $\mathbf{x} \in \text{Im } \pi_K$, we have the identity

$$\|\mathbf{x}\|^2 = \|\mathcal{F}_{L,K}\mathbf{x}\|^2 + \|\mathcal{F}_{L^c,K}\mathbf{x}\|^2. \quad (51)$$

We think of $\mathcal{F}_{L,K}$ as a map from \mathbb{C}^K to \mathbb{C}^J , with singular values $s_1 \leq \dots \leq s_p$, where $p = |K|$, and $\mathcal{F}_{L^c,K}$ as a map from \mathbb{C}^K to \mathbb{C}^J , with singular values $t_1 \leq \dots \leq t_p$. Using the observations above, we see that

$$\begin{aligned} s_j^2 &= \min_{\{S \subset \mathbb{C}^K: \dim S=j\}} \max_{\mathbf{x} \in S: \mathbf{x} \neq \mathbf{0}} \frac{\|\mathcal{F}_{L,K}\mathbf{x}\|^2}{\|\mathbf{x}\|^2} \\ &= \min_{\{S \subset \mathbb{C}^K: \dim S=j\}} \max_{\mathbf{x} \in S: \mathbf{x} \neq \mathbf{0}} \left[1 - \frac{\|\mathcal{F}_{L^c,K}\mathbf{x}\|^2}{\|\mathbf{x}\|^2} \right] \\ &= 1 - \max_{\{S \subset \mathbb{C}^K: \dim S=j\}} \min_{\mathbf{x} \in S: \mathbf{x} \neq \mathbf{0}} \frac{\|\mathcal{F}_{L^c,K}\mathbf{x}\|^2}{\|\mathbf{x}\|^2} \\ &= 1 - t_{p-j+1}^2. \end{aligned} \quad (52)$$

□

References

- [1] D. A. BARMHERZIG AND J. SUN, *Low-photon holographic phase retrieval*. OSA Imag. Appl. Opt. Cong. (2020), pp. 1-2.
- [2] D. A. BARMHERZIG, J. SUN, P. LI, T. J. LANE, AND E. J. CANDÈS, *Holographic phase retrieval and reference design*, Inv. Prob., 35 (2019), pp. 194001.
- [3] A. BARNETT, *How exponentially ill-conditioned are contiguous submatrices of the Fourier matrix?*, ArXiv, arXiv:2004.09643 (2020), pp. 1–24.
- [4] A. BARNETT, C. L. EPSTEIN, L. GREENGARD, J. MAGLAND, *Geometry of the phase retrieval problem*, ArXiv, arXiv:1808.10747 (2018), pp. 1–33.

- [5] H. H. BAUSCHKE, P. L. COMBETTES, AND D. R. LUKE, *Phase retrieval, error reduction algorithm, and Fienup variants: a view from convex optimization*, J. Opt. Soc. Am. A, 19 (2002), pp. 1334–1345.
- [6] Y. BRUCK AND L. SODIN, *On the ambiguity of the image reconstruction problem*, Optics Communications, 30 (1979), pp. 304–308.
- [7] H. N. CHAPMAN ET AL, *Femtosecond diffractive imaging with a soft-x-ray free-electron laser*, Nat. Phys., 2 (2006), pp. 839–843.
- [8] H. N. CHAPMAN, A. BARTY, S. MARCHESINI, A. NOY, S. P. HAU-RIEGE, C. CUI, M. R. HOWELLS, R. ROSEN, H. HE, J. C. H. SPENCE, U. WEIERSTALL, T. BEETZ, C. JACOBSEN, AND D. SHAPIRO, *High-resolution ab initio three-dimensional x-ray diffraction microscopy*, J. Opt. Soc. Am. A, 23 (2006), pp. 1179–1200.
- [9] K. HE, M. K. SHARMA, AND O. COSSAIRT, *High dynamic range coherent imaging using compressed sensing*, Opt. Exp., 23 (2015), pp. 30904–30906.
- [10] V. ELSE, I. RANKENBURG, AND P. THIBAUT, *Searching with iterated maps*, Proceedings of the National Academy of Sciences, 104 (2007), pp. 418–423.
- [11] A. FANNJIANG AND T. STROHMER, *The Numerics of phase retrieval*, ArXiv, arXiv:2004.05788 (2020), pp. 1–83.
- [12] J. R. FIENUP, *Phase retrieval algorithms: a comparison*, Applied Optics, 21 (1982), pp. 2758–2769.
- [13] W. FUCHS, *On the eigenvalues of an integral equation arising in the theory of band-limited signals*, Jour. Math. Anal. and Appl., 9 (1964), pp. 317–330.
- [14] M. HAYES, *The reconstruction of a multidimensional sequence from the phase or magnitude of its Fourier transform*, IEEE Transactions on Acoustics, Speech, and Signal Processing, 30 (1982), pp. 140–154.
- [15] J. MIAO, P. CHARALAMBOUS, J. KIRZ, AND D. SAYRE, *Extending the methodology of x-ray crystallography to allow imaging of micrometre-sized non-crystalline specimens*, Nature, 400 (1999), pp. 342–334.
- [16] C. METZLER, P. SCHNITER, A. VEERARAGHAVAN, AND R. BARANIUK, *prDeep: Robust phase retrieval with a flexible deep network*, ICML, 35 (2018), pp. 3501–3510.

- [17] Y. NISHINO, J. MIAO, AND T. ISHIKAWA, *Image reconstruction of nanostructured nonperiodic objects only from oversampled hard x-ray diffraction intensities*, Phys. Rev. B, 68 (2003), p. 220101.
- [18] Y. SHECHTMAN, Y. C. ELDAR, O. COHEN, H. N. CHAPMAN, J. MIAO, AND M. SEGEV, *Phase retrieval with application to optical imaging: a contemporary overview*, IEEE Sig. Proc. Mag., 32 (2015), pp. 87–109.
- [19] B. SHI, Q. LIAN, X. HUANG, AND N. AN, *Constrained phase retrieval: when alternating projection meets regularization*, J. Opt. Soc. Am. B, 35 (2018), pp. 1271–1281.
- [20] D. SLEPIAN, *Prolate spheroidal wave functions, Fourier analysis, and uncertainty– V: the discrete case*, Bell System Technical Journal, 57 (1978), pp. 1371–1430.
- [21] D. SLEPIAN AND H. O. POLLAK, *Prolate spheroidal wave functions, Fourier analysis, and uncertainty, I*, Bell System Technical Journal, 40 (1961), pp. 43–63.

D.A. BARMHERZIG: dbarmherzig@flatironinstitute.org
A.H. BARNETT: abarnett@flatironinstitute.org
C.L. EPSTEIN: cle@math.upenn.edu
L.F. GREENGARD: lgreengard@flatironinstitute.org
J.F. MAGLAND: jmagland@flatironinstitute.org
M. RACHH: mrachh@flatironinstitute.org